

FORMATION OF OVERHEATED REGIONS AND TRUNCATED DISKS AROUND BLACK HOLES; THREE-DIMENSIONAL GENERAL RELATIVISTIC RADIATION-MAGNETOHYDRODYNAMICS SIMULATIONS

HIROYUKI R. TAKAHASHI¹, KEN OHSUGA^{2,3} TOMOHISA KAWASHIMA¹, AND YUICHIRO SEKIGUCHI⁴,
to be submitted to ApJ

ABSTRACT

Using three-dimensional general relativistic radiation magnetohydrodynamics simulations of accretion flows around stellar mass black holes, we report that the relatively cold disk ($\gtrsim 10^7\text{K}$) is truncated near the black hole. Hot and less-dense regions, of which the gas temperature is $\gtrsim 10^9\text{K}$ and more than ten times higher than the radiation temperature (overheated regions), appear within the truncation radius. The overheated regions also appear above as well as below the disk, and sandwich the cold disk, leading to the effective Compton upscattering. The truncation radius is $\sim 30r_g$ for $\dot{M} \sim L_{\text{Edd}}/c^2$, where $r_g, \dot{M}, L_{\text{Edd}}, c$ are the gravitational radius, mass accretion rate, Eddington luminosity, and light speed. Our results are consistent with observations of very high state, whereby the truncated disk is thought to be embedded in the hot rarefied regions. The truncation radius shifts inward to $\sim 10r_g$ with increasing mass accretion rate $\dot{M} \sim 100L_{\text{Edd}}/c^2$, which is very close to an innermost stable circular orbit. This model corresponds to the slim disk state observed in ultra luminous X-ray sources. Although the overheated regions shrink if the Compton cooling effectively reduces the gas temperature, the sandwich-structure does not disappear at the range of $\dot{M} \lesssim 100L_{\text{Edd}}/c^2$. Our simulations also reveal that the gas temperature in the overheated regions depends on black hole spin, which would be due to efficient energy transport from black hole to disks through the Poynting flux, resulting gas heating.

Subject headings: accretion, accretion disks — magnetohydrodynamics (MHD) — black hole physics

1. INTRODUCTION

It is widely believed that the black hole accretion flows are the central engine of the luminous compact objects like active galactic nuclei and black hole binaries (BHs). The X-ray spectra of such objects are mainly composed of the soft component and the power-law component. The soft component is dominant over the power-law component in the high-soft state as well as in the slim disk state, and, in contrast, the power-law component is quite prominent in the low-hard state and in the very high state (see, Done et al. 2007, and references therein). The soft component is accepted to be multi-color disk blackbody, which is emitted from the relatively cold, optically thick accretion disk. On the other hand, the power-law component is thought to be produced due to the Compton upscattering in the hot and less-dense regions (so-called disk corona). From the observational point of view, Done & Kubota (2006) suggested the several models for the disk corona, and Kubota & Done (2004) reported the cold disk is truncated around the black hole and the flow within the truncation radius is consist of the hot gas. However, both the structure and the formation mechanism of the hot, rarefied plasma around the cold disk is not understood yet.

The most important mechanism to heat up the matter around the black hole is the dissipation of the magnetic energy. Since a part of the kinetic energy of the accretion flow is converted to the magnetic energy via the magnetorotational instability, the dissipation of the enhanced magnetic energy works to increase the gas temperature. Indeed, this mechanism is thought to be origin of the viscous heating in the accretion disk. However, the radiative cooling prevents the gas from the rising in the gas temperature in the dense regions. Thus, study by the magnetohydrodynamics (MHD) is insufficient and we need the radiation-MHD (RMHD). The formation of the hot, rarefied regions above the cold disk has been reported by the RMHD simulations of a local patch of the disk (Hirose et al. 2006), the global RMHD simulations (Ohsuga et al. 2009; Ohsuga & Mineshige 2011) and the general relativistic (GR) RMHD simulations (Sądowski & Narayan 2015). However, the dependency of the mass accretion rate hasn't been investigated well enough yet.

In addition, the rotation of the black hole might cooperate the heating of the gas around the black hole. The rotational energy of the black hole is extracted and transported outward by the Poynting flux. If the transported electromagnetic energy is dissipated in the less dense regions, the gas temperature would drastically increase. This should be resolved by the GRRMHD simulations.

In this paper, by performing the three-dimensional GRRMHD simulations, we study the formation of the hot, rarefied regions around the black holes. We will show that the relatively cold disk is truncated around the black hole and the flow becomes very hot within the truncation radius. The hot, rarefied regions also appear

¹ Center for Computational Astrophysics, National Astronomical Observatory of Japan, Mitaka, Tokyo 181-8588, Japan

² Division of Theoretical Astronomy, National Astronomical Observatory of Japan, Mitaka, Tokyo 181-8588, Japan

³ School of Physical Sciences, Graduate University of Advanced Study (SOKENDAI), Shonan Village, Hayama, Kanagawa 240-0193, Japan

⁴ Department of Physics, Toho University, Funabashi, Chiba 274-8510, Japan

above the cold disk. In addition, we study the change of the size and the gas temperature of the hot regions due to the difference of the mass accretion rate and the black hole spin. In §2, basic equations and numerical method are described. We present our results in §3. In this section, we also discuss about the Compton cooling based on the comparison between the cooling and dynamical timescales, since the Compton cooling is not taken into account in our simulations. It is reported by Sądowski & Narayan (2015) that the Compton cooling strongly impacts on the gas temperature. Finally §4 is devoted to summary and discussion.

2. BASIC EQUATIONS AND NUMERICAL METHOD

In the present work, we numerically solve the GR-RMHD equations. We hereafter take light speed c as unity. The Greek suffixes indicate space-time components, and the Latin suffixes indicates space components. The mass conservation equation is given by

$$(\rho u^\nu)_{;\nu} = 0, \quad (1)$$

where ρ is the proper mass density, u^μ is the fluid four velocity. The energy momentum conservation for the magnetofluid is given by

$$(T_\mu^\nu + M_\mu^\nu)_{;\nu} = G_\mu, \quad (2)$$

where G_μ is the radiation four force (see equation [14]). The energy momentum tensor for fluid T_μ^ν is given by

$$T_\mu^\nu = (\rho + e + p_{\text{gas}}) u_\mu u^\nu + p_{\text{gas}} \delta_\mu^\nu, \quad (3)$$

where $\delta_{\mu\nu}$ is the Kronecker delta, e is the gas internal energy, and p_{gas} is the gas pressure. Here we assume simple Γ -law for the equation of state and thus $e = (\Gamma - 1)p_{\text{gas}}$. We take $\Gamma = 5/3$ in the following. The energy momentum tensor for electromagnetic field $M^{\mu\nu}$ is given by

$$M^{\mu\nu} = F^{\mu\alpha} F_\alpha^\nu - \frac{1}{4} g^{\mu\nu} F^{\alpha\beta} F_{\alpha\beta}, \quad (4)$$

where $F^{\mu\nu}$ is the electromagnetic tensor and $g^{\mu\nu}$ is the metric tensor. Here we absorbed factor $\sqrt{4\pi}$ into definition of $F^{\mu\nu}$. In this paper, we adopted non resistive magnetohydrodynamics, so that $F^{\mu\nu}$ satisfies

$$u_\mu F^{\mu\nu} = 0. \quad (5)$$

The magnetic four-vector is defined using magnetic field tensor $F^{\mu\nu}$ as

$$b^\mu = \frac{1}{2} \epsilon^{\mu\nu\kappa\lambda} u_\nu F_{\kappa\lambda}, \quad (6)$$

where $\epsilon^{\mu\nu\kappa\lambda}$ is the Levi-Chivita tensor. Substituting equation (6) into (4) gives more simple form;

$$M^{\mu\nu} = b^2 u^\mu u^\nu + p_{\text{mag}} g^{\mu\nu} - b^\mu b^\nu, \quad (7)$$

where $p_{\text{mag}} = b^2/2$ is the magnetic pressure. Since the components of b^μ are not independent, it is useful to define magnetic field three vector $B^i \equiv F^{*it}$, where $F^{*\mu\nu}$ is the dual of electromagnetic tensor. Then we obtain

$$b^t = B^i u^i g_{i\mu}, \quad (8)$$

$$b^i = \frac{B^i + b^t u^i}{u^t}. \quad (9)$$

Using these expressions, the induction equation $F_{;\nu}^{*\mu\nu} = 0$ gives

$$\partial_j (\sqrt{-g} B^j) = 0, \quad (10)$$

$$\partial_t (\sqrt{-g} B^i) + \partial_j [\sqrt{-g} (b^i u^j - b^j u^i)] = 0, \quad (11)$$

where $g = \det(g_{\mu\nu})$.

The energy momentum conservation for the radiation field is given by

$$R_{\mu;\nu}^\nu = -G_\mu, \quad (12)$$

where R_μ^ν is the radiation energy momentum tensor. In this paper, we employed M-1 formalism to close equations. Then, the radiation energy momentum tensor is given by

$$R^{\mu\nu} = 4p_{\text{rad}} u_{\text{rad}}^\mu u_{\text{rad}}^\nu + p_{\text{rad}} g_{\mu\nu}, \quad (13)$$

where p_{rad} is the radiation pressure and u_{rad}^μ is the radiation frame's four velocity (Levermore 1984; Sądowski et al. 2013; Kanno et al. 2013). The radiation four force G^μ is given by

$$G^\mu = -\rho \kappa_{\text{abs}} (R_\alpha^\mu u^\alpha + 4\pi B u^\mu) - \rho \kappa_{\text{sca}} (R_\alpha^\mu u^\alpha + R_\beta^\alpha u_\alpha u^\beta u^\mu), \quad (14)$$

where κ_{abs} and κ_{sca} are the opacities for absorption and scattering. We employ free-free emission/absorption and isotropic electron scattering,

$$\kappa_{\text{abs}} = 6.4 \times 10^{22} \rho T_{\text{gas}}^{-\frac{7}{2}} \text{ cm}^2 \text{ g}^{-1}, \quad (15)$$

$$\kappa_{\text{sca}} = 0.4 \text{ cm}^2 \text{ g}^{-1}, \quad (16)$$

where T_{gas} is the gas temperature, which is related to the gas pressure as

$$p_{\text{gas}} = \frac{\rho k_B T_{\text{gas}}}{\mu m_p}. \quad (17)$$

Here k_B and m_p are the Boltzmann constant and the proton mass, and $\mu = 0.5$ is the mean molecular weight. The blackbody intensity is given by $B = a_{\text{rad}} T_{\text{gas}}^4 / 4\pi$, where a_{rad} is the radiation constant.

We solve these equations in Boyer-Lindquist polar coordinate (t, r, θ, ϕ) in Kerr-Schild space-time with black hole mass $M_{\text{BH}} = 10M_\odot$, where M_\odot is the solar mass. Numerical grid points are $(N_r, N_\theta, N_\phi) = (264, 264, 64)$ and computational domain consists of $r = [r_{\text{H}}, 250r_{\text{g}}]$, $\theta = [0, \pi]$, and $\phi = [0, 2\pi]$, where r_{H} is the horizon radius and $r_{\text{g}} = GM_{\text{BH}}$ is the gravitational radius. The radial grid size exponentially increases with radius. The θ is given by $\theta = \pi x_2 + (1 - h) \sin(2\pi x_2)/2$ where $h = 0.2$ and x_2 is the uniform grid between 0 and 1 (Gammie et al. 2003). We adopted outflow boundary conditions at inner and outer radial boundaries ($r = r_{\text{H}}$ and $250r_{\text{g}}$). Reflective boundary condition is adopted at the polar axis ($\theta = 0$ and π).

The advection term is solved explicitly using Lax-Friedrich method, while the source term describing interaction between the gas and the radiation is integrated implicitly (Roedig et al. 2012; Takahashi et al. 2013; Takahashi & Ohsuga 2013; McKinney et al. 2014; Sądowski et al. 2014). The divergence-free condition for the magnetic field is satisfied by applying Flux-CT method (Tóth 2000).

We start simulation from the equilibrium torus given by Fishbone & Moncrief (1976). The inner edge of the torus is situated at $r = 20r_g$, while the radius where the pressure has its maximum value is $33r_g$. The initial torus is not in local thermodynamic equilibrium ($T_{\text{gas}} \neq T_{\text{gas}}$), but we set small radiation energy density $E_{\text{rad}} = 10^{-10}$ uniformly (but, see Sądowski et al. 2014). Here $T_{\text{rad}} = (\hat{E}_{\text{rad}}/a_{\text{rad}})^{1/4}$ is the radiation temperature, and the hat denotes the quantity in comoving frame.

The inner edge of the torus locates at $r = 20r_g$ and there is a pressure maximum at $r = 33r_g$. The maximum density of the torus ρ_0 is taken to be a parameter. All physical quantities are normalized using ρ_0 and r_g . The time is normalized by r_g/c , so that the unit time is $\simeq 5 \times 10^{-5}$ s for $10M_\odot$ black hole. We embedded the weak poloidal magnetic field inside the torus. The magnetic flux vector A_ϕ is given by $A_\phi \propto \rho$ and the ratio of the maximum b^2 and p_{gas} at the initial state is taken to be 100. In addition to the torus, we set the thin, unmagnetized hot atmosphere. The density and gas pressure profile of the atmosphere are given by $\rho = 10^{-4}\rho_0(r/r_g)^{-1.5}$ and $p_{\text{gas}} = 10^{-6}\rho_0(r/r_g)^{-2.5}$.

In this paper, we perform three simulations. We set $(\rho_0, a^*) = (10^{-4}\text{g cm}^{-3}, 0)$ for run A, $(10^{-2}\text{g cm}^{-3}, 0)$ for run B, and $(10^{-4}\text{g cm}^{-3}, 0.9375)$ for run C.

3. RESULTS

3.1. overview of simulations

In all simulations, the poloidal magnetic field lines in the torus begin to be twisted due to the differential rotation after the simulations start. The toroidal component of the magnetic fields is enhanced. The angular momentum is transported as the magnetorotational instability grows up inside the torus, leading the mass accretion onto the black hole. Then, the mass accretion rate suddenly increases and the quasi-steady accretion disks are produced around the black hole.

Figure 1 shows the time evolution of the mass accretion rate \dot{M} . We find the rapid increase of the accretion rate at around $t = 0.06$ s. Then, a part of the initial torus reaches to the black hole. At $t \gtrsim 0.06$ s, the accretion rate does not largely change, although a transient amplification appears at $t \sim 0.17$ s for run B (see black line). Such an amplification is caused by the accretion of the dense matter of the initial torus.

As shown in this figure, the mass accretion rate for run A (red line) is much larger than that for runs B and C, since the larger ρ_0 is employed. The accretion rate highly exceeds the critical rate, L_{Edd} , so that the radiation pressure-dominated disk is produced and the strong jets are launched from the disk surface via the radiation force. The overall structure of the accretion disk and jets at $t = 0.3$ s is shown in Figure 2, where the disk is presented as blue-white-red volume rendering and the elongated white-red regions indicate the jets. Thin lines are magnetic field lines. We find that the toroidal magnetic fields are amplified inside the disk. The disk-jet structure in this model is roughly consistent with that by Ohsuga et al. (2009); Takeuchi et al. (2010); Ohsuga & Mineshige (2011); McKinney et al. (2014); Takahashi & Ohsuga (2015); Sądowski et al. (2015). For run B and run C, the geometrical thickness of the disks

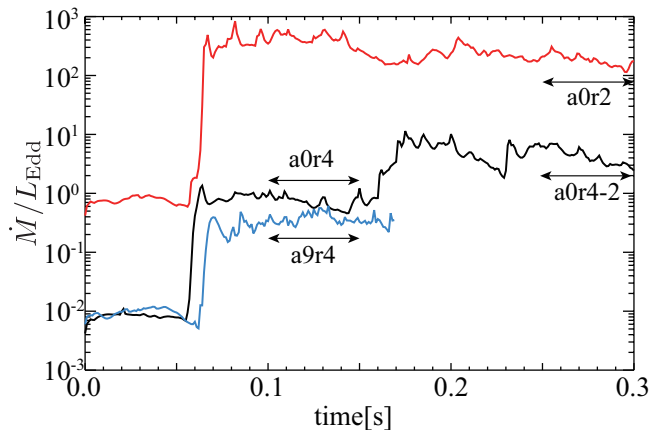


FIG. 1.— Time evolution of mass accretion rate. Black, red, and blue lines show results of runs A, B, and C, respectively. Arrows show the time interval for time average. It is relatively small (see below), since the mass accretion rate is comparable to or slightly smaller than the critical rate.

3.2. structure of overheated region

We here take the time average between $t = [0.1, 0.15]$ s for run C (model a9r4), $t = [0.25, 0.3]$ s for run A (model a0r2), and $t = [0.1, 0.15]$ s (model a0r4) as well as $t = [0.25, 0.3]$ s (model a0r4-2) for run B. The time averaged mass accretion rate of model a0r4 ($0.73L_E$) is close to that of model a9r4 ($0.38L_E$), so that we can discuss about the effect of the rotation of the black hole by comparing these two models. Here, we note that the inflow-outflow equilibrium is achieved within $r \sim 15r_g$ in two models (see, table 1). On the other hand, we use models a0r2 and a0r4-2 in order to investigate the difference of the disk structure due to the difference of the mass accretion rate, since the mass accretion rates are quite different, $4.3L_E$ (a0r4-2) and $430L_E$ (a0r2). In both models, the flow is in inflow-outflow equilibrium within $r \sim 20r_g$.

Here, we define following averages of a physical quantity $f = f(t, r, \theta, \phi)$. The azimuthal average:

$$\langle f \rangle_{w,\phi} = \frac{\int d\phi \sqrt{-g} f w}{\int_0^{2\pi} d\phi \sqrt{-g} w}, \quad (18)$$

and the azimuthal and polar average:

$$\langle f \rangle_{w,\theta\phi} = \frac{\int d\phi d\theta \sqrt{-g} f w}{\int d\theta d\phi \sqrt{-g} w}, \quad (19)$$

where w is a weight function. In this paper, we used a mass density as a weight function ($\langle \dots \rangle_\rho$), or we take an average without a weight function ($\langle \dots \rangle_1$).

In Figure 3 the ϕ -averaged density and gas temperature profiles are plotted on $r - \theta$ plane. We find that the geometrical thickness of the high-density region (white region on the right) at $r \lesssim 10r_g$ is very large for model a0r2 and is relatively small for the other models. This is caused by the difference of the mass accretion rate, $\dot{M} \gg L_{\text{Edd}}$ for model a0r2 and $\dot{M} \lesssim L_{\text{Edd}}$ for the other models. In this figure, we find the gas temperature tends to be high (low) in the low (high) density regions. The temperature in the high-density regions is around 10^7 K, and, on the other hand, is larger than 10^9 K in the less dense regions.

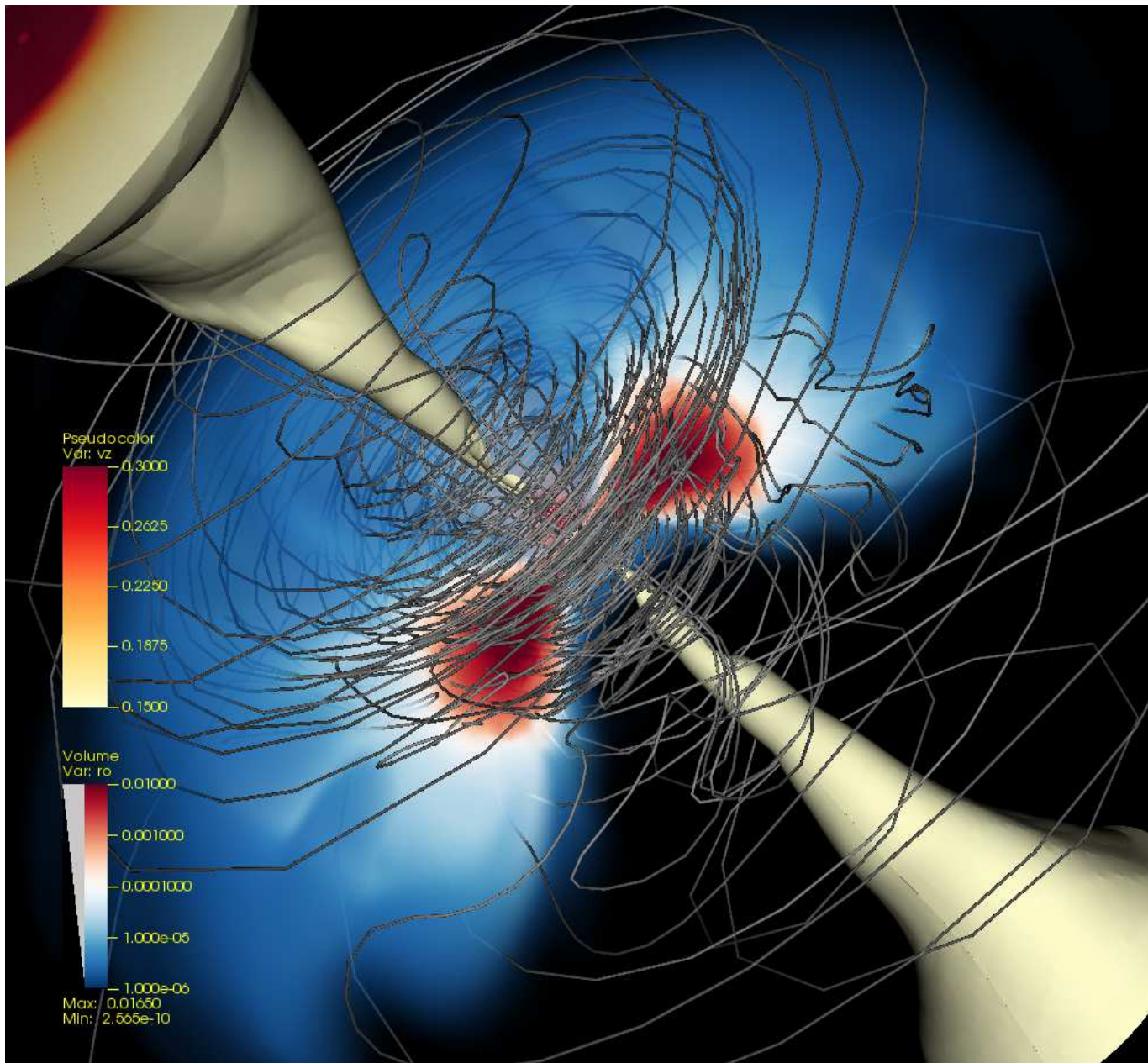


FIG. 2.— Global structure of radiation dominated accretion disks near the black hole at $t = 0.3$ s (run B). The figure shows the density (blue-white-red volume rendering), the outflow velocity (white-red volume data), and the magnetic field lines (gray lines).

In this figure, the black solid lines show the photosphere ($\tau_{\text{tot}} = 1$), and the dashed lines mean the surface where the effective optical depth, τ_{eff} , becomes unity. Here these optical depths are calculated from the polar axis,

$$\tau_{\text{tot}} = \int_0^\theta \gamma \rho (\kappa_{\text{abs}} + \kappa_{\text{sca}}) \sqrt{g_{\theta\theta}} d\theta', \quad (20)$$

and

$$\tau_{\text{eff}} = \int_0^\theta \gamma \rho \sqrt{(\kappa_{\text{abs}} + \kappa_{\text{sca}}) \kappa_{\text{sca}}} \sqrt{g_{\theta\theta}} d\theta', \quad (21)$$

(McKinney et al. 2014). In all models, the opening angle of the photosphere is not large, $\sim 25^\circ$ for model a0r2 and $\sim 55^\circ$ for the other models. Since the absorption opacity is much smaller than the scattering opacity, the effective

optical depth is less than the total optical depth. Thus, the surface of $\tau_{\text{eff}} = 1$ appears deep inside the photosphere. This figure also shows that the disk of $\tau_{\text{eff}} > 1$ is truncated around the black hole. The truncation radius r_{tr} , at which the surface of $\tau_{\text{eff}} = 1$ reaches to the equatorial plane, is $r_{\text{tr}} \sim 30r_g$ for the low- ρ_0 models (a0r4, a0r4-2, a9r4), and $r_{\text{tr}} \sim 10r_g$ for the high- ρ_0 models (a0r2). It implies that the inner part of the disk does not emit the blackbody radiation.

The seed photons emitted at the surface of $\tau_{\text{eff}} = 1$ suffer from the numerous scattering before escaping from the photosphere. The Compton upscattering would play an important role for producing the hard X-ray photons, since the gas is very hot ($\gtrsim 10^9$ K) in the regions between the photosphere and the surface of $\tau_{\text{eff}} = 1$. Hereafter we call this hot regions “overheated regions”. As we will

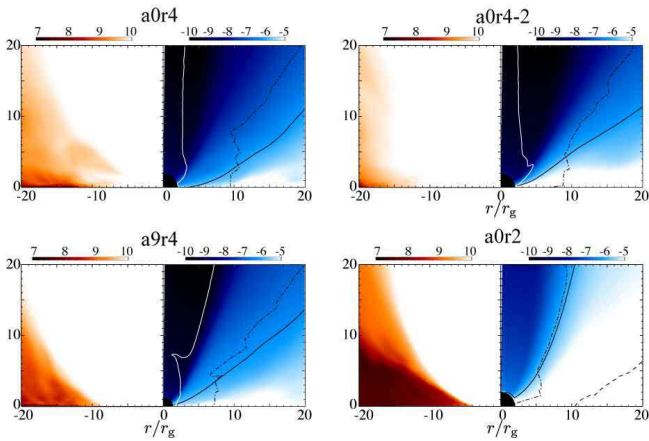


FIG. 3.— The ϕ -averaged density (right) and gas temperature (left) profiles for each models. Black solid lines indicate the photosphere, where $\tau_{\text{tot}} = 1$, and the effective optical depth is unity on the dashed lines. Dot-dashed lines show where the dynamical time is comparable to the Compton cooling time, so that the Compton cooling might effectively work below the lines. White lines denote expected surface where the gas temperature decreases down to 10^{10} K due to the Compton cooling.

show below, the gas is not in LTE and we find $T_{\text{gas}} \gtrsim 10T_{\text{rad}}$ in the overheated regions.

Figure 4 shows the gas temperature distribution on the equatorial plane. In each panels, the time averaged T_{gas} is shown in the left half and the right half of the panels indicates the snapshot at the end of the range of the time, $t = 0.15$ (a0r4-2 and a0r2) and $t = 0.3$ (a0r4 and a9r4). Time averaged contours where $T_{\text{gas}}/T_{\text{rad}} = 10$ are plotted by white solid lines in the right half in each panels. Black circles indicate an innermost stable circular orbit (ISCO).

This figure shows that the gas temperature increases as approaching to the black hole. Although the gas temperature is $\sim 10^7$ K for a larger radius (blue), it exceeds 10^9 K around the black hole (green, yellow, and red). This hot region corresponds to the overheated region on the equatorial plane. Although the line are complicated in the models of a0r4 and a9r4, T_{gas} is comparable to or slightly larger than T_{rad} in the blue regions, and is at least ten times larger than T_{rad} in the overheated regions.

In comparison with the model a0r4 (upper-left), the gas temperature for the model a9r4 (lower-left) is very high in the vicinity of the black hole. Although the red region appears within $r \sim 7r_g$ in the case of a9r4, such a very hot region is not produced for the model a0r4. In contrast, the gas temperatures in two models are approximately equal in the regions of $r \gtrsim 10r_g$. These results imply the rotation of the black hole contributes to the heating of the gas around the black hole (we will discuss later). Also, the right panels indicate the overheated region shrinks as the accretion rate increases. The diameter of the overheated region is about $14r_g$ for the model a0r2 and $40r_g$ for the model a0r4-2. The overheated region extends to the outside of the ISCO for low- ρ_0 models (a0r4, a0r4-2, a9r4).

The profiles of the gas and radiation temperatures are more clearly understood in Figure 5, where we plot $\langle T_{\text{gas}} \rangle_{\rho, \theta, \phi}$ (solid) and $\langle T_{\text{rad}} \rangle_{\rho, \theta, \phi}$ (dashed) as a function of the radius. Red, orange, black and blue lines show results of models a0r4, a0r4-2, a0r2, and a9r4, respectively. It is found that the radiation temperature is insensitive to the radius. For the model a0r2, we find

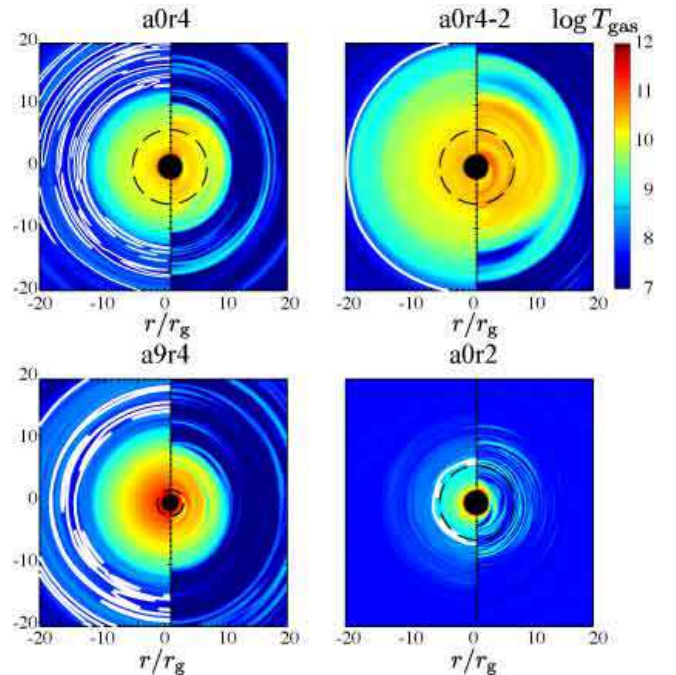


FIG. 4.— Gas temperature profile on the equatorial plane. In each panels, the time averaged T_{gas} and T_{gas} at $t = t_{\text{end}}$ are plotted on the right and left, respectively. White lines represent where $T_{\text{gas}}/T_{\text{rad}} = 10$. Black dashed lines indicate the ISCO.

$\langle T_{\text{rad}} \rangle_{\rho, \theta, \phi} \sim 4 \times 10^7$ K. The radiation temperature for the other models is slightly lower than that of a0r2. The gas temperature is comparable to the radiation temperature at $r \gtrsim 25r_g$ for low- ρ_0 models (a0r4, a9r4, a0r4-2) and at $r \gtrsim 10r_g$ for a high- ρ_0 model (a0r2). As approaching the black hole, the gas temperature steeply increases and deviates from the radiation temperature. The radius of the overheated region (r_{over}), at which $T_{\text{gas}} = 10T_{\text{rad}}$, is about $15r_g$ for models a0r4 and a9r4, $20r_g$ for model a0r4-2, and $7r_g$ for model a0r2.

As we have already mentioned above, the radius of the overheated region depends on the mass accretion rate. Comparing models a0r2 ($\dot{M} \sim 430L_{\text{Edd}}$) and a0r4-2 ($\dot{M} \sim 4.3L_{\text{Edd}}$), we find r_{over} for a0r2 is less than that for a0r4-2. This figure also shows that the gas temperatures is insensitive to the rotation of the black hole at $r \gtrsim 10r_g$ (see a0r4 and a9r4). However, the gas is more effectively heated up in the case of a9r4. In this model, the maximum temperature exceeds 10^{11} K near the black hole, and is 10 times larger than that of a0r4. Although the gas temperature might be overestimated since the Compton cooling is not taken into consideration in the present simulations, our results indicate that the rotation of the black hole contributes to the heating of the gas in the vicinity of the black hole.

So far, we have discussed with using the time- and/or angle-averaged structures. However, our three-dimensional simulations show a non-axisymmetric structure, which are smeared out by taking the average. The right half of each panels in Figure 4 is the snapshot of the gas temperature. We can see patchy structure and/or spiral hot regions in all models. Such a non-uniform structure would impact on the variability of observed spectra (Chan et al. 2015).

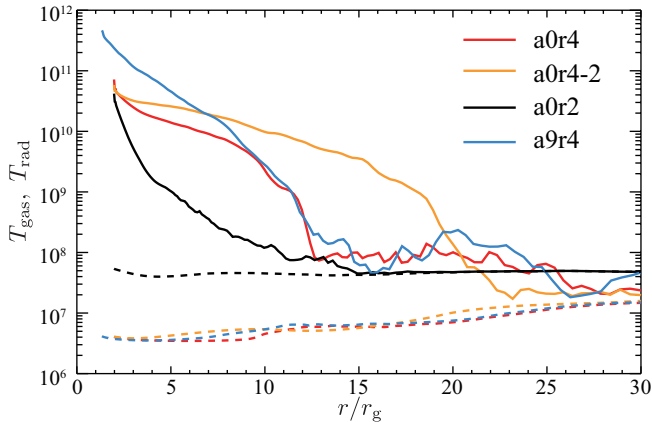


FIG. 5.— Radial profiles of $\langle T_{\text{gas}} \rangle_{\rho, \theta, \phi}$ (solid) and $\langle T_{\text{rad}} \rangle_{\rho, \theta, \phi}$ (dashed). Red, orange, black and blue lines show results of models a0r4, a0r4-2, a0r2, and a9r4, respectively.

3.3. formation mechanisms of overheated region

Figure 6 shows the ratio of the inflow time, t_{in} , and the cooling time, t_{cool} , for models a0r4 (red solid), a0r4-2 (orange solid), a0r2 (black solid), and a9r4 (blue solid). These time scales are evaluated as

$$t_{\text{in}}(r) = - \int_{r_{\text{H}}}^r \frac{dr'}{\langle v_r \rangle_{\rho, \theta, \phi}}, \quad (22)$$

(McKinney et al. 2014), and

$$t_{\text{cool}} = \left\langle \frac{e}{4\pi\kappa_{\text{abs}}\mathbf{B}} \right\rangle_{\rho, \theta, \phi}. \quad (23)$$

We can see that the $t_{\text{in}}/t_{\text{cool}}$ is larger for a larger radius. Close to the black hole, the inflow speed increases with decreasing radius, so that t_{in} is reduced. In addition, the cooling time becomes longer for the inner region since the mass density decreases. As a consequence, the gas accretes onto the black hole without cooling, producing the overheated region (Beloborodov 1998).

Why does the truncation radius shift inward as the mass accretion rate increases? This is simply understood by the density dependence of the cooling time. Since we employ the free-free absorption opacity, $\rho\kappa_{\text{abs}} \propto \rho^2$, in the present work, the cooling time is in inverse proportion to the density, $t_{\text{cool}}[\propto e/(\rho\kappa_{\text{abs}})] \propto \rho^{-1}$. The larger ρ_0 is, the larger the density of the disk and the mass accretion rate becomes. Thus, the overheated region shrinks as the mass accretion rate increases.

Next, we discuss about the reason why the maximum gas temperature in the overheated region is higher for the case of the rotating black hole (a9r4) than for the case of the non-rotating black hole (a0r4). The one of the most plausible mechanism is that the rotational energy of the rotating black hole is transmitted to the matter around the black hole. When the black hole threaded by the magnetic field rotates, its rotational energy is extracted through the magnetic field (Blandford & Znajek 1977; McKinney & Gammie 2004; Tanabe & Nagataki 2008). This process enhances the energy of the black hole magnetosphere and induces the launching of the jets (McKinney 2006; Penna et al. 2010; Tchekhovskoy et al. 2012; McKinney et al. 2013).

Figure 7 shows the radial component of the Poynting flux $\langle -M_t^r \rangle_{>1, \phi}$ normalized by ρ_0 for model a0r4 (left)

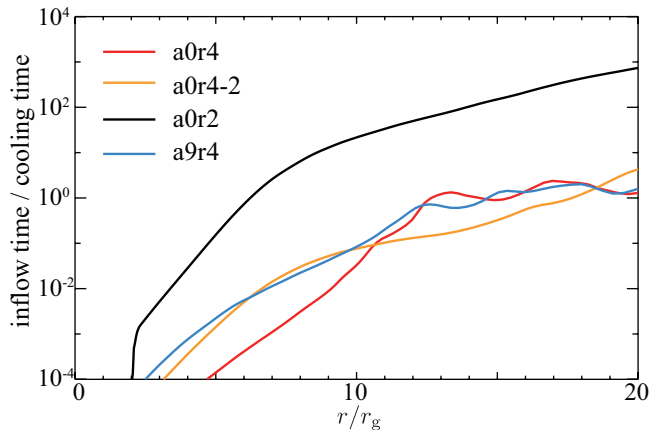


FIG. 6.— Radial profiles of the ratio of inflow time and cooling time. The inflow time is calculated by the equation (24) and the cooling time is estimated based on the free-free emission. Red, orange, black and blue lines show results of models a0r4, a0r4-2, a0r2, and a9r4, respectively.

and a9r4 (right). It is found in this figure that the Poynting flux is outward in most of the region. Also, we find that the electromagnetic energy is more effectively transported outward for the rotating black hole than for the non-rotating black hole. This is conspicuous near the black hole. Indeed, white regions appear only around the rotating black hole (see right panel). For the rotating black hole case, the strong Poynting flux is mainly emitted to the direction of $\theta \sim \pi/4$ and $3\pi/4$. In addition, we find the substantial Poynting flux in the direction along the equatorial plane, $\theta \sim \pi/2$. The electromagnetic energy transported via the Poynting flux would work to heat up the matter in the overheated regions.

In Figure 8, we plot the outward Poynting flux, $\langle -M_t^r \rangle_{>1, \phi}$ (black solid), inward radiation flux, $\langle R_t^r \rangle_{>1, \phi}$ (red dashed), and inward thermal energy flux, $\langle \Gamma p_{\text{gas}} u_t u^r / (\Gamma - 1) \rangle_{>1, \phi}$ (orange dashed) at $r = 5r_g$ as a function of θ . Top and bottom panels show results for a0r4 and a9r4. This figure shows that the gas energy flux dominates the radiation energy flux in both models, since the gas is overheated and its temperature much exceeds the radiation temperature at around $r = 5r_g$ (see Figures 4 and 5).

As shown in this figure, the outward Poynting flux becomes larger for the rotating black hole case than that for the non-rotating black hole case. This is because that the rotational energy is extracted from the rotating black hole through the magnetic field. The outward Poynting energy flux should increase as increasing the black hole spin a^* . Since the electromagnetic energy is dissipated around the black hole, the gas temperature in the overheated region becomes higher in the case of the rotating black hole. We note that the ideal magnetohydrodynamics is assumed in the present simulations, so that the dissipation of the magnetic energy might be originated from the numerical resistivity.

Another possible mechanism of the energy dissipation is the mode conversion of the MHD waves. The Alfvén waves excited around the black hole propagates inside the accretion disks. Since the density contrast exists inside the disks, Alfvén waves would suffer from the mode conversion to the fast and slow modes due to the non-linear effects (Goldstein 1978; Terasawa et al. 1986). The

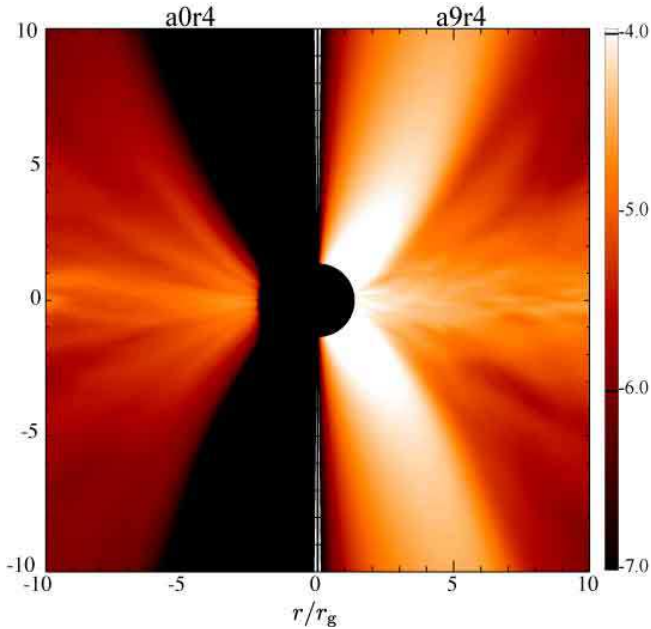


FIG. 7.— Profiles of the outward Poynting flux $\langle -M_t^r \rangle_{1,\phi}$ around the non-rotating black hole (a0r4) and the rotating black hole (a9r4).

generated compressional waves would heat up the gas (Takamoto et al. 2012).

3.4. compton cooling

In the present simulations, the Compton cooling is not included. The Compton upscattering works to produce the high-energy photons, and at the same time induces the cooling of the gas. On the dot-dashed lines in Figure 3, the dynamical timescale,

$$t_{\text{dyn}} = \left\langle \frac{r}{v_r} \right\rangle_{1,\phi}, \quad (24)$$

equals to the Compton cooling timescale,

$$t_{\text{comp}} = \left\langle -\frac{e}{\rho \kappa_{\text{sca}} \hat{E}_{\text{rad}} \frac{4k_B(T_{\text{exp}} - T_{\text{rad}})}{m_e}} \right\rangle_{1,\phi}, \quad (25)$$

where $T_{\text{exp}} = 10T_{\text{rad}}$. Thus the t_{comp} indicates the time scale that the gas temperature decreases to $T_{\text{gas}} = T_{\text{exp}}$. Here note that the result does not change even if we set T_{gas} to be $5T_{\text{rad}}$.

Below the dot-dashed lines, the gas is cooled by the Compton cooling. In contrast, the gas is overheated above the lines, $T_{\text{gas}} > 10T_{\text{rad}}$. That is, even if the Compton cooling effectively works, the hard X-ray photons are produced by the Compton upscattering in the regions between the solid line and the dot-dashed line (narrowed overheated regions). The radius of the narrowed overheated region near the equatorial plane is $\sim 10r_g$ for models a0r4, a9r4, and a0r4-2. For the model of a0r2, the narrowed overheated regions does not appear on the equatorial plane. Although the Compton cooling also reduces the truncation radius, the disk truncation does not disappear. We find $r_{\text{tr}} \sim 10r_g$ (a0r4, a9r4, and a0r4-2) and $r_{\text{tr}} \sim 4r_g$ (a0r2).

In Figure 3, the gas temperature is much higher than 10^{10}K in wide regions (white in the left panels). How-

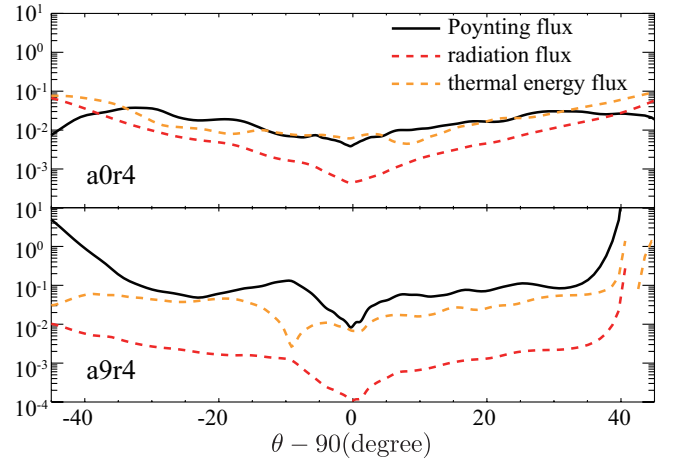


FIG. 8.— Radial component of the energy fluxes at $r = 5r_g$ for a0r4 (top) and a9r4 (bottom). Black solid lines show the outward Poynting flux, while orange and red dashed lines show the inward thermal energy flux and the radiation flux, respectively.

ever, the gas temperature in this region would be less than 10^{10}K in reality, except for near the polar axis for models a0r4 a0r4-2, and a9r2. This is due to the Compton cooling. The white lines in Figure 3 show where the dynamical time (equation 24) becomes comparable to the cooling time, which is estimated by setting $T_{\text{exp}} = 10^{10}\text{K}$ in equation (25). For models a0r4, a0r4-2 and a9r4, we find that the gas temperature is thought to be $\gtrsim 10^{10}\text{K}$ at the vicinity of the polar axis (between the rotation axis and the white line), while it is expected to be $\lesssim 10^{10}\text{K}$ in the outer region. We also note that the region where $T_{\text{gas}} > 10^{10}\text{K}$ disappears for the high \dot{M} case (a0r2). Our results are consistent with Sądowski & Narayan (2015), in which the very hot regions do not form via the Compton cooling for the case of $\dot{M} \gtrsim 100L_{\text{Edd}}$.

We can conclude that, even if the Compton cooling effectively decreases the gas temperature, the disk of $\tau_{\text{eff}} > 1$ is truncated around the black hole and is sandwiched by the overheated regions (between the solid line and the dot-dashed line in Figure 3), enhancing the hard X-ray spectra via the Compton upscattering in the overheated regions.

4. SUMMARY & DISCUSSION

By performing three-dimensional GRRMHD simulations of accretion flows around the black holes, we revealed that the relatively cold disk, of which the gas and the radiation temperatures are \sim several $\times 10^7\text{K}$ and the effective optical depth is > 1 , is truncated at around the black hole. The hot and rarefied regions (overheated regions), in which the gas temperature ($T_{\text{gas}} > 10^9\text{K}$) is more than ten times higher than the radiation temperature, appear within the truncation radius and above the cold disk. The cold disk is sandwiched by the overheated regions, so that the hard X-ray photons would be produced by the Compton upscattering in the overheated regions. The truncation radius decreases with an increase of the mass accretion rate, since the cooling is effective in the dense disk. In the present simulations, it is $\sim 30r_g$ for the case of $\dot{M} \sim L_{\text{Edd}}$ and $\sim 10r_g$ for the case of $\dot{M} \sim 100L_{\text{Edd}}$. Although the overheated regions shrink if the Compton cooling effectively reduces

TABLE 1
TYPICAL RADIUS OBTAINED BY SIMULATIONS

model	inflow-outflow equilibrium	r_{over}	r_{tr}
a0r4	~ 15	$\sim 15(10)$	$\sim 30(9)$
a9r4	~ 15	$\sim 15(10)$	$\sim 30(7)$
a0r4-2	~ 20	$\sim 20(10)$	$\sim 30(9)$
a0r2	~ 20	$\sim 7(2)$	$\sim 10(4)$

NOTE. — From left to right, model, the size of the inflow-outflow equilibrium, the equatorial radius of the overheated region, and the equatorial radius where $\tau_{\text{eff}} = 1$. The value denoted in the bracket is obtained by taking into account the Compton cooling. These radii are denoted in the unit of r_g .

the gas temperature, the sandwich-structure does not disappear at the range of $\dot{M} \sim 1 - 100L_{\text{Edd}}$. The maximum gas temperature in the overheated region is about ten times higher for the rotating black hole than for the non-rotating black hole. In the case of the rotating black hole, since the electromagnetic energy is enhanced at the very vicinity of the black hole and transported outward by the Poynting flux, the matter would be effectively heated up.

Our low- ρ_0 models would explain the very high state of the BHBs. The very high state is thought to appear for the near- or sub-Eddington case, and the power-low component is dominant over the soft component. Kubota & Done (2004) reported that the inner part of the optically-thick disk does not reach to the ISCO radius in this state, and the effective Compton upscattering produces the strong power-low spectra. Such features nicely fit our results of models a0r4, a0r4-2, and a9r4, whereby the truncated disk is sandwiched by the overheated regions. On the other hand, our model a0r2 would correspond to the slim disk state. Vierdayanti et al. (2008) succeeded in reproducing the observed X-ray spectra of the ultra luminous X-ray source, using the slim disk model which is not truncated. In our super-Eddington model (a0r2), the truncation radius is very close to the ISCO radius, so that our result is not inconsistent with the observations.

Here we note that, the multi-frequency radiation transfer calculations are needed to accurately investigate the emergent spectra. Such calculations are attempted by Kawashima et al. (2012) in which the hard X-ray spectra is obtained by performing the post-processing radiation transfer calculations including the Compton upscattering and down-scattering (see Zhu et al. 2015; Narayan et al. 2015). However, it is difficult to accurately treat the gas-radiation interaction via the Compton process in the hydrodynamics simulations. In Kawashima et al. (2009), the Compton heating/cooling is calculated by solving the Kompaneets equation based on the assumption that the radiation has a blackbody spectrum. Recently, Sądowski & Narayan (2015) also performed hy-

drodynamics simulations taking into account the Comptonization. In their method, the assumption of the blackbody spectrum is relaxed and the conservation of number of photons is carefully treated. However, as long as the Kompaneets equation is employed, the simulations would induce some inaccuracies in the regions of anisotropic radiation fields like around the photosphere. Multi-frequency RMHD simulations are necessary to resolve this problem, but such simulations are too time consuming to perform.

The time for simulations is limited in the present work as shown in Figure 1, especially for run C. The structure of the magnetic fields might change by graduation due to the magnetic dynamo. If it does, the structure of the overheated regions is influenced. Thus, the long-term three-dimensional simulations should be explored in future work, since it is well known that no magnetic dynamo works in the axisymmetric calculations. Two-dimensional simulations including the sub-grid dynamo model is another way Sądowski et al. (2015).

Simulations of higher resolution are left as important future work. In order to revolve the magnetorotational instability, it has been reported that $Q_\theta \gtrsim 6$ is required (McKinney et al. 2014). Here, Q_θ is evaluated as $Q_\theta = \lambda_{\text{MRI}}/rd\theta$ with $d\theta$ being the grid size in theta direction (Hawley et al. 2013; McKinney et al. 2014). In model a0r4, in which the disk is the thinnest in the present work, $\langle Q_\theta \rangle_{\rho, \theta\phi}$ is $\simeq 7$ around $r = 10r_g$. This value is comparable to the required value of 6, so that it is better to perform simulations with small $d\theta$.

Finally, M-1 closure method employed in the present work is known to be somewhat problematic in the optically very thin or moderately thin regions. The accurate radiation fields can be obtained by solving radiation transfer equations. Such a method has been proposed by Jiang et al. (2014); Ryan et al. (2015); Ohsuga & Takahashi (2016)

Numerical computations were carried out on Cray XC30 at the Center for Computational Astrophysics of National Astronomical Observatory of Japan, on FX10 at Information Technology Center of the University of Tokyo, and on K computer at AICS. This work is supported in part by JSPS Grant-in-Aid for Scientific Research (C) (15K05036 K.O., 15H00782 Y.S.). A part of this research has been funded by MEXT HPCI STRATEGIC PROGRAM and the Center for the Promotion of Integrated Sciences (CPIS) of Sokendai.

REFERENCES

- Beloborodov, A. M. 1998, MNRAS, 297, 739
 Blandford, R. D. & Znajek, R. L. 1977, MNRAS, 179, 433
 Chan, C.-K., Psaltis, D., Özel, F., Narayan, R., & Sądowski, A. 2015, ApJ, 799, 1
 Done, C., Gierliński, M., & Kubota, A. 2007, A&A Rev., 15, 1
 Done, C. & Kubota, A. 2006, MNRAS, 371, 1216
 Fishbone, L. G. & Moncrief, V. 1976, ApJ, 207, 962
 Gammie, C. F., McKinney, J. C., & Tóth, G. 2003, ApJ, 589, 444
 Goldstein, M. L. 1978, ApJ, 219, 700
 Hawley, J. F., Richers, S. A., Guan, X., & Krolik, J. H. 2013, ApJ, 772, 102
 Hirose, S., Krolik, J. H., & Stone, J. M. 2006, ApJ, 640, 901
 Jiang, Y.-F., Stone, J. M., & Davis, S. W. 2014, ApJS, 213, 7
 Kanno, Y., Harada, T., & Hanawa, T. 2013, PASJ, 65, 72
 Kawashima, T., Ohsuga, K., Mineshige, S., Heinzeller, D., Takabe, H., & Matsumoto, R. 2009, PASJ, 61, 769

- Kawashima, T., Ohsuga, K., Mineshige, S., Yoshida, T., Heinzeller, D., & Matsumoto, R. 2012, *ApJ*, 752, 18
- Kubota, A. & Done, C. 2004, *MNRAS*, 353, 980
- Levermore, C. D. 1984, *J. Quant. Spec. Radiat. Transf.*, 31, 149
- McKinney, J. C. 2006, *MNRAS*, 368, 1561
- McKinney, J. C. & Gammie, C. F. 2004, *ApJ*, 611, 977
- McKinney, J. C., Tchekhovskoy, A., & Blandford, R. D. 2013, *Science*, 339, 49
- McKinney, J. C., Tchekhovskoy, A., Sadowski, A., & Narayan, R. 2014, *MNRAS*, 441, 3177
- Narayan, R., Zhu, Y., Psaltis, D., & Sadowski, A. 2015, *ArXiv e-prints*
- Ohsuga, K. & Mineshige, S. 2011, *ApJ*, 736, 2
- Ohsuga, K., Mineshige, S., Mori, M., & Kato, Y. 2009, *PASJ*, 61, L7+
- Ohsuga, K. & Takahashi, H. R. 2016, *ApJ*, 818, 162
- Penna, R. F., McKinney, J. C., Narayan, R., Tchekhovskoy, A., Shafee, R., & McClintock, J. E. 2010, *MNRAS*, 408, 752
- Roedig, C., Zanotti, O., & Alic, D. 2012, *MNRAS*, 426, 1613
- Ryan, B. R., Dolence, J. C., & Gammie, C. F. 2015, *ApJ*, 807, 31
- Sądowski, A. & Narayan, R. 2015, *MNRAS*, 454, 2372
- Sądowski, A., Narayan, R., McKinney, J. C., & Tchekhovskoy, A. 2014, *MNRAS*, 439, 503
- Sądowski, A., Narayan, R., Tchekhovskoy, A., Abarca, D., Zhu, Y., & McKinney, J. C. 2015, *MNRAS*, 447, 49
- Sądowski, A., Narayan, R., Tchekhovskoy, A., & Zhu, Y. 2013, *MNRAS*, 429, 3533
- Takahashi, H. R. & Ohsuga, K. 2013, *ApJ*, 772, 127
- . 2015, *PASJ*, 67, 60
- Takahashi, H. R., Ohsuga, K., Sekiguchi, Y., Inoue, T., & Tomida, K. 2013, *ApJ*, 764, 122
- Takamoto, M., Inoue, T., & Inutsuka, S.-i. 2012, *ApJ*, 755, 76
- Takeuchi, S., Ohsuga, K., & Mineshige, S. 2010, *PASJ*, 62, L43+
- Tanabe, K. & Nagataki, S. 2008, *Phys. Rev. D*, 78, 024004
- Tchekhovskoy, A., McKinney, J. C., & Narayan, R. 2012, *Journal of Physics Conference Series*, 372, 012040
- Terasawa, T., Hoshino, M., Sakai, J.-I., & Hada, T. 1986, *J. Geophys. Res.*, 91, 4171
- Tóth, G. 2000, *Journal of Computational Physics*, 161, 605
- Vierdayanti, K., Watarai, K.-Y., & Mineshige, S. 2008, *PASJ*, 60, 653
- Zhu, Y., Narayan, R., Sadowski, A., & Psaltis, D. 2015, *MNRAS*, 451, 1661